ISSN 1560-3547, Regular and Chaotic Dynamics, 2018, Vol. 23, No. 6, pp. 654–664. © Pleiades Publishing, Ltd., 2018.

Moser's Quadratic, Symplectic Map[1)]

Arnd Bäcker[1,2*] and James D. Meiss[3]**

[1] *Technische Universität Dresden, Institut für Theoretische Physik and Center for Dynamics, 01062 Dresden, Germany*

[2] *Max-Planck-Institut für Physik komplexer Systeme, Nöthnitzer Strasse 38, 01187 Dresden, Germany*

[3] *Department of Applied Mathematics, University of Colorado, Boulder, CO 80309-0526, USA*

Received August 22, 2018; accepted September 12, 2018

Abstract—In 1994, Jürgen Moser generalized Hénon's area-preserving quadratic map to obtain a normal form for the family of four-dimensional, quadratic, symplectic maps. This map has at most four isolated fixed points. We show that the bounded dynamics of Moser's six parameter family is organized by a codimension-three bifurcation, which we call a *quadfurcation*, that can create all four fixed points from none.

The bounded dynamics is typically associated with Cantor families of invariant tori around fixed points that are doubly elliptic. For Moser's map there can be two such fixed points: this structure is not what one would expect from dynamics near the cross product of a pair of uncoupled Hénon maps, where there is at most one doubly elliptic point. We visualize the dynamics by escape time plots on 2D planes through the phase space and by 3D slices through the tori.

MSC2010 numbers: 37J40, 70H08, 34C28, 37C05

DOI: 10.1134/S1560354718060023

Keywords: Hénon map, symplectic maps, saddle-center bifurcation, Krein bifurcation, invariant tori

1. INTRODUCTION

Moser derived a normal form for quadratic symplectic maps on a $2n$-dimensional vector space in 1994 [1]. For $n = 1$ the normal form is conjugate to the famous and well-studied Hénon map [2]. In contrast, the dynamics of the Moser map for $n \geqslant 2$ have not yet been explored. In [3] we started the investigation of the $n = 2$ case, i. e., the four-dimensional quadratic symplectic map. Perhaps one of the most intriguing of its features is the possibility of a *quadfurcation*, in which four new solutions are created out-of-nowhere under parameter variation. Of particular interest are the possible combinations of stability configurations; in particular, the case when two of the fixed points are elliptic-elliptic and two are elliptic-hyperbolic is surprising, as this would not be possible when the different degrees of freedom are not coupled.

Symplectic maps naturally arise as Poincaré maps of Hamiltonian flows and therefore are relevant for many different applications, for example in the dynamics of the solar system and galaxies [4–9], beam dynamics of particle accelerators [10–13], plasma physics [14], and chemistry [15–20]. Investigating the simplest prototypical examples, such as the area-preserving Hénon map or Chirikov's standard map in the two-dimensional case, helps to give a good understanding of the way in which dynamical properties depend on parameters in typical maps. Thus the study of the dynamics of Moser's four-dimensional, quadratic symplectic map is of fundamental interest as it describes the generic local behavior of symplectic maps in 4D.

[1)] Supplementary materials are available for this article at https://doi.org/10.1134/S1560354718060023 and are accessible for authorized users.

[*] E-mail: arnd.baecker@tu-dresden.de

[**] E-mail: jdm@colorado.edu

2. NORMAL FORM

As Moser showed [1], every quadratic symplectic map on $\mathbb{R}^{2n}$ can be written as the composition of an affine symplectic map, a symplectic shear, $\sigma : \mathbb{R}^n \times \mathbb{R}^n \to \mathbb{R}^n \times \mathbb{R}^n$, of the form

$$\sigma(x, y) = \big(x, y - \nabla V(x)\big), \tag{2.1}$$

and a linear symplectic map. When the map is quadratic, $V : \mathbb{R}^n \to \mathbb{R}$ is a cubic potential.

For the two-dimensional case, the map can be transformed by an affine coordinate change to the form

$$H(x, y) = (-y + a_{\mathrm{h}} + x^2, x) \tag{2.2}$$

with a single parameter a_{h}. For $a_{\mathrm{h}} < 1$ this map has two fixed points $(x, y) = (x^*_\pm, x^*_\pm)$, with

$$x^*_\pm = 1 \pm \sqrt{1 - a_{\mathrm{h}}}. \tag{2.3}$$

These fixed points are created in a saddle-center bifurcation when $a_{\mathrm{h}} = 1$ at $(x^*, y^*) = (1, 1)$. When $a_{\mathrm{h}} < 1$, the fixed point (x^*_+, x^*_+) is hyperbolic. When $-3 < a_{\mathrm{h}} < 1$, the negative branch is linearly stable (elliptic), and the map is conjugate to the map introduced by Hénon [21]. At $a_{\mathrm{h}} = -3$ the lower fixed point undergoes a period-doubling bifurcation, and below this parameter value both fixed points are unstable. It has been shown that there are no bounded orbits outside the square $S = \{|x| \leqslant x^*_+, |y| \leqslant x^*_+\}$ [22]. Figure 1 illustrates the dynamics for two different parameters using an escape time plot: for a grid of initial points the time needed to leave the square S is encoded in color. Points that stay inside S for 10^4 iterations are shown in white. The elliptic fixed point is surrounded by invariant tori, as predicted by the Kolmogorov – Arnold – Moser (KAM) theorem. Some of these tori are shown as grey curves. In the right panel, one can also see a period-five orbit and some of the surrounding invariant circles that form a resonance zone.

By applying a similar coordinate change, Moser showed in [1] that the quadratic symplectic map in $\mathbb{R}^4$ can generically be written in an analogous normal form. Transforming this slightly by shifting the coordinates and parameters [3], this map can be written as

$$(\xi', \eta') = M(\xi, \eta) = \Big(\xi + C^{-T}\big(-\eta + C\xi + \nabla U(\xi)\big), C\xi\Big). \tag{2.4}$$

Here $\xi \equiv (\xi_1, \xi_2) \in \mathbb{R}^2$, $\eta \equiv (\eta_1, \eta_2) \in \mathbb{R}^2$ are canonically conjugate coordinates and momenta, respectively, and

$$C = \begin{pmatrix} \alpha & \beta \\ \gamma & \delta \end{pmatrix}, \tag{2.5}$$

$$U = a\xi_1 + b\xi_2 + \tfrac{1}{2}c\xi_1^2 + \varepsilon_2\xi_1^3 + \xi_1\xi_2^2. \tag{2.6}$$

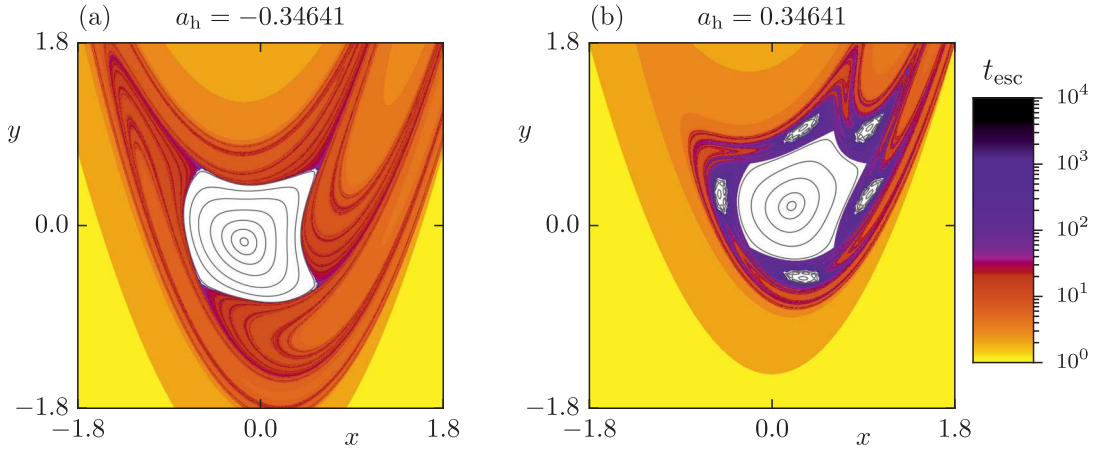

Fig. 1. Escape time plot for the Hénon map for $a_{\mathrm{h}} = -0.34641$ (left) and $a_{\mathrm{h}} = 0.34641$ (right). Some regular tori are shown as grey curves.

The map has two discrete parameters, $\varepsilon_1 \equiv \det(C) = \alpha\delta - \beta\gamma \ = \pm 1$, and $\varepsilon_2 \equiv \pm 1$ or 0. The remaining six parameters are free and are conveniently grouped into (a, b, c), determining the location of the fixed points (together with ε_2) and (α, δ, μ), determining (together with ε_1) the stability properties. Here we define

$$\mu = \beta + \gamma \tag{2.7}$$

from which the off-diagonal elements of C follow by

$$\beta, \gamma = \tfrac{1}{2}\mu \pm \sqrt{\varepsilon_1 - \alpha\delta + \mu^2/4}. \tag{2.8}$$

As shown in [3], the choice of sign for β and γ is unimportant. Note that (2.8) has real solutions only when $\mu^2 \geqslant 4(\alpha\delta - \varepsilon_1)$, and that C is symmetric, $\beta = \gamma = \mu/2$, only at the lower bound of this inequality.

3. THE QUADFURCATION

The fixed points (ξ^*, η^*) of the map (2.4) correspond to critical points of the cubic polynomial (2.6). Thus the coordinates ξ^* satisfy

$$0 = \nabla U(\xi^*) = \begin{pmatrix} a + c\xi_1^* + 3\varepsilon_2 \xi_1^{*2} + \xi_2^{*2} \\ b + 2\xi_1^*\xi_2^* \end{pmatrix}. \tag{3.1}$$

The momenta are then given by $\eta^* = C\xi^*$. The case $a = b = c = 0$ is an organizing center for the solutions of (3.1). In this case the second component immediately implies that either $\xi_1^* = 0$ or $\xi_2^* = 0$, and then, whenever $\varepsilon_2 \neq 0$, the first implies that both $\xi_1^* = \xi_2^* = 0$. We call this the *quadfurcation point*. Since the matrix elements (α, δ, μ) are still free, this occurs on a codimension-three surface in the six-dimensional parameter space. There are at most four fixed points except when $\varepsilon_2 = 0$, which has a line of fixed points when $a = b = c = 0$. For simplicity we will assume in this paper that $\varepsilon_2 \neq 0$ (the case $\varepsilon_2 = 0$ is discussed in [3]).

More generally, if $b \neq 0$, then (3.1) implies that $\xi_1^* \neq 0$, so

$$\xi_2^* = -\frac{b}{2\xi_1^*}.$$

Substituting into the first component of (3.1) then shows that ξ_1^* must be a root of the scalar polynomial

$$P(v) = 3\varepsilon_2 v^4 + cv^3 + av^2 + \tfrac{1}{4}b^2. \tag{3.2}$$

When $\varepsilon_2 \neq 0$, this polynomial is quartic, so there are at most four roots. Since the linear term vanishes, there is exactly one only at the quadfurcation point $a = b = c = 0$.

There are various regions in the (a, b, c) parameter space that have different numbers of fixed points. As we discuss below, of particular interest are paths through the quadfurcation point along which four new solutions are created out of nowhere.

The stability of a fixed point is characterized by Broucke's parameters [23, 24] $A = \mathrm{tr}(DM)$ and $B = \frac{1}{2}\left((\mathrm{tr}(DM))^2 - \mathrm{tr}(DM^2)\right)$, where DM is the linearized map at the fixed point. There are seven stability regions in the (A, B)-plane bounded by the saddle-center (SC) line

$$SC = B - 2A + 2 = 0, \tag{3.3}$$

where there is a double eigenvalue $\lambda_1 = \lambda_2 = 1$, the period-doubling (PD) line

$$PD = B + 2A + 2 = 0, \tag{3.4}$$

where there is a double eigenvalue $\lambda_1 = \lambda_2 = -1$, and the Krein parabola (KP)

$$KP = B - A^2/4 - 2 = 0, \tag{3.5}$$

where there are two sets of double eigenvalues on the unit circle or real line. These regions are shown in Fig. 2. The stability type of a fixed point is labeled by combinations of E (elliptic), H

(hyperbolic), and I (inverse hyperbolic). For example, EH denotes a point with one elliptic and one hyperbolic pair of eigenvalues. The seventh case, denoted CU (complex unstable), occurs in the region $KP > 0$ and corresponds to a Krein quartet of complex eigenvalues.

Figure 2 shows a quadfurcation that initially creates two EE and two EH fixed points. The curves trace out the stability of the four fixed points along the parameter path

$$(a, b, c) = \Delta(1.0, 0.25, 0.5) \tag{3.6}$$

with $\Delta \in [-0.5, 0]$, and the remaining parameters given in the caption. For this matrix, the four fixed points are born on the SC line where the eigenvalues are 1, 1, and $\frac{1}{2}(-1 \pm \sqrt{3}\mathrm{i})$, and emerge along paths that are tangent to this line. This tangency holds generically for curves in parameter space that go through the quadfurcation point. The EE point indicated by the red curve in the figure eventually loses stability by period-doubling (for $\Delta = -0.31745$), becoming IE, and that shown in blue loses stability by a Krein bifurcation (for $\Delta = -0.21536$), becoming CU.

The quadfurcation occurs on the SC line in Fig. 2, and this is true more generally. Indeed, when $a = b = c = 0$, the values of A and B are

$$\begin{aligned} A^{\mathrm{Q}} &= 4 - \varepsilon_1(\beta - \gamma)^2, \\ B^{\mathrm{Q}} &= 6 - 2\varepsilon_1(\beta - \gamma)^2, \end{aligned} \tag{3.7}$$

and this point lies on the line defined by (3.3). Thus, the position along the line depends primarily upon $\beta - \gamma$, the asymmetric part of C (2.5). When C is symmetric, the quadfurcation occurs at $(A^{\mathrm{Q}}, B^{\mathrm{Q}}) = (4, 6)$, which corresponds to a quartet of unit eigenvalues. If C is asymmetric and $\varepsilon_1 = 1$, it occurs below this point. The quadfurcation then creates one pair of fixed points below $SC = 0$, of type EH or IH, and one above $SC = 0$, (initially) of type EE or IE. When $\varepsilon_1 = -1$, the quadfurcation occurs above $(4, 6)$ on the SC line and there will be two fixed points (initially) of type HH and two of type EH. A quadfurcation can directly lead to CU fixed points only when C is symmetric. However, if C is asymmetric, then it is possible for an EE or an HH fixed point to undergo a Krein bifurcation at some parameter value after it is created, recall the blue curve

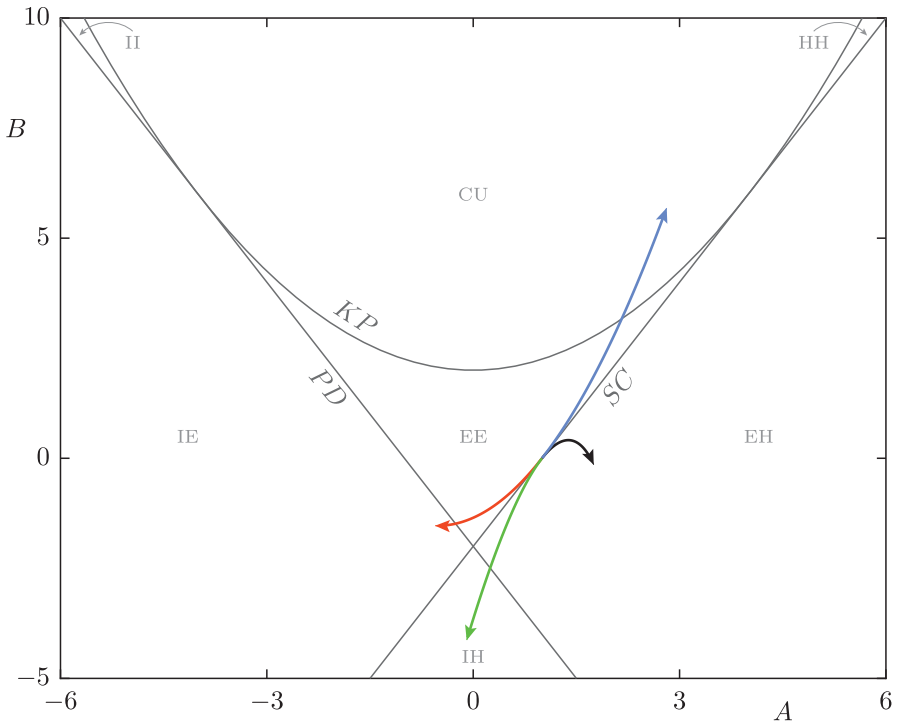

Fig. 2. Stability parameters of the four fixed points in the (A, B) plane created in the transition, $\emptyset \to 2$ EE + 2 EH for $\Delta < 0$ along the path (3.6) with $(\alpha, \mu, \delta) = (1, 1, 0.5)$ and $\varepsilon_1 = \varepsilon_2 = 1$. Since $|\beta - \gamma| = \sqrt{3}$, (3.7) implies that the quadrupling occurs at $(A^{\mathrm{Q}}, B^{\mathrm{Q}}) = (1, 0)$.

Table 1. Location of the quadfurcation along the SC line (column one) and stabilities of the created fixed points (columns four and five). These stabilities are valid for a path of the form $(a, b, c) = \Delta(a^*, b^*, c^*)$ which has a quadfurcation at $\Delta = 0$. For $\varepsilon_2 = 1$, four fixed points are created as a becomes negative provided that $a < -\sqrt{3}|b|$. When $\varepsilon_2 = -1$, two fixed points exist whenever a or $b \neq 0$; these collide at $\Delta = 0$. The special case $\beta = \gamma$ is not shown here.

$(A^{\mathrm{Q}}, B^{\mathrm{Q}})$	Condition		Fixed Points and Stability	
on SC	ε_1	$\lvert\beta - \gamma\rvert$	$\varepsilon_2 = 1$, $a < -\sqrt{3}\lvert b\rvert$	$\varepsilon_2 = -1$, a or $b \neq 0$
$> (4, 6)$	-1	$\neq 0$	2 EH + 2 HH	2 HH
$< (4, 6)$	1	< 2	2 EE + 2 EH	2 EH
$= (0, -2)$	1	2	IE + EE + IH + EH	IH + EH
$< (0, -2)$	1,	> 2	2 IE + 2 IH	2 IH

in Fig. 2. The different stability combinations that arise from quadfurcations along lines in (a, b, c) space, like that in (3.6), are summarized in Table 1, see [3] for details.

4. GEOMETRY — ELLIPTIC BUBBLES

Of particular interest are those parameters of the Moser map that lead to doubly-elliptic (EE) fixed points. As expected from Kolmogorov – Arnold – Moser theory [25], when the twist is nondegenerate, such fixed points should be surrounded by a Cantor family of two-tori on which the dynamics is conjugate to incommensurate rotation. The result that shows this for the 2D case is Moser's twist theorem [26]. It implies that the density of these tori approaches one as they limit on an elliptic point provided that the linearized frequency is not in a low-order resonance. We have not been able to find a statement of a similar result for higher-dimensional maps, though results along these lines have been proven for elliptic equilibria of Hamiltonian flows [27, 28].

Motion on these invariant tori is, of course, bounded; but just as for the Hénon map, most orbits of the Moser map are unbounded. Indeed, one can show that when $\varepsilon_2 \neq 0$, there exists a radius κ such that if two successive points fall outside the ball, $\|\xi_t\|, \|\xi_{t+1}\| > \kappa$, then the orbit is unbounded (An upper bound for κ is obtained in [3]). One way to display the transition between bounded and unbounded motion is an escape time plot, similar to that for the Hénon map in Fig. 1: initial points are iterated until they leave the ball of radius κ, and the required time to escape is encoded in color. To visualize this, we consider a grid of initial conditions on a 2D plane in phase space, and plot the escape time for each point using a color scale.

Figure 3 shows escape time plots for the quadfurcation of Fig. 2 for a sequence of Δ values along the path (3.6) as Δ varies, with the matrix C held fixed. Here we use the 2D plane of initial conditions $(\xi, \eta) = (\xi, C\xi)$ that contains all four fixed points of (2.4). These are shown in the figures by $\times$ symbols. After the quadfurcation, the regions near the four fixed points that are "bounded" are colored white: these correspond to orbits with numerically computed escape times larger than 10^4. The bounded orbits appear to be primarily associated with EE-EH pairs, each leading to a structure reminiscent of that of the 2D Hénon map shown in Fig. 1, though now this structure is seen in the two-plane $\eta = C\xi$ instead of the full phase space. The elliptic-elliptic fixed points are surrounded by regions of predominantly regular motion (see below). One interesting feature, not possible for a 2D map, is that even "within" a region of regular motion one finds orbits that can escape; for example, there is a ring of escaping orbits near the right EE fixed point in 3(c). Indeed, a linearly stable, elliptic fixed point can be unstable due to Arnold's transition chain mechanism [29–32]. Numerically one sees that resonances between the oscillation frequencies of surrounding tori lead to chaotic zones and drift along resonant channels leads to additional escape routes.

To help visualize the geometry of regular tori, we can also use a 3D phase space slice [33]. For this we define new coordinates (ξ, χ), with $\chi = \eta - C\xi$, so that the fixed points lie in the 2D plane

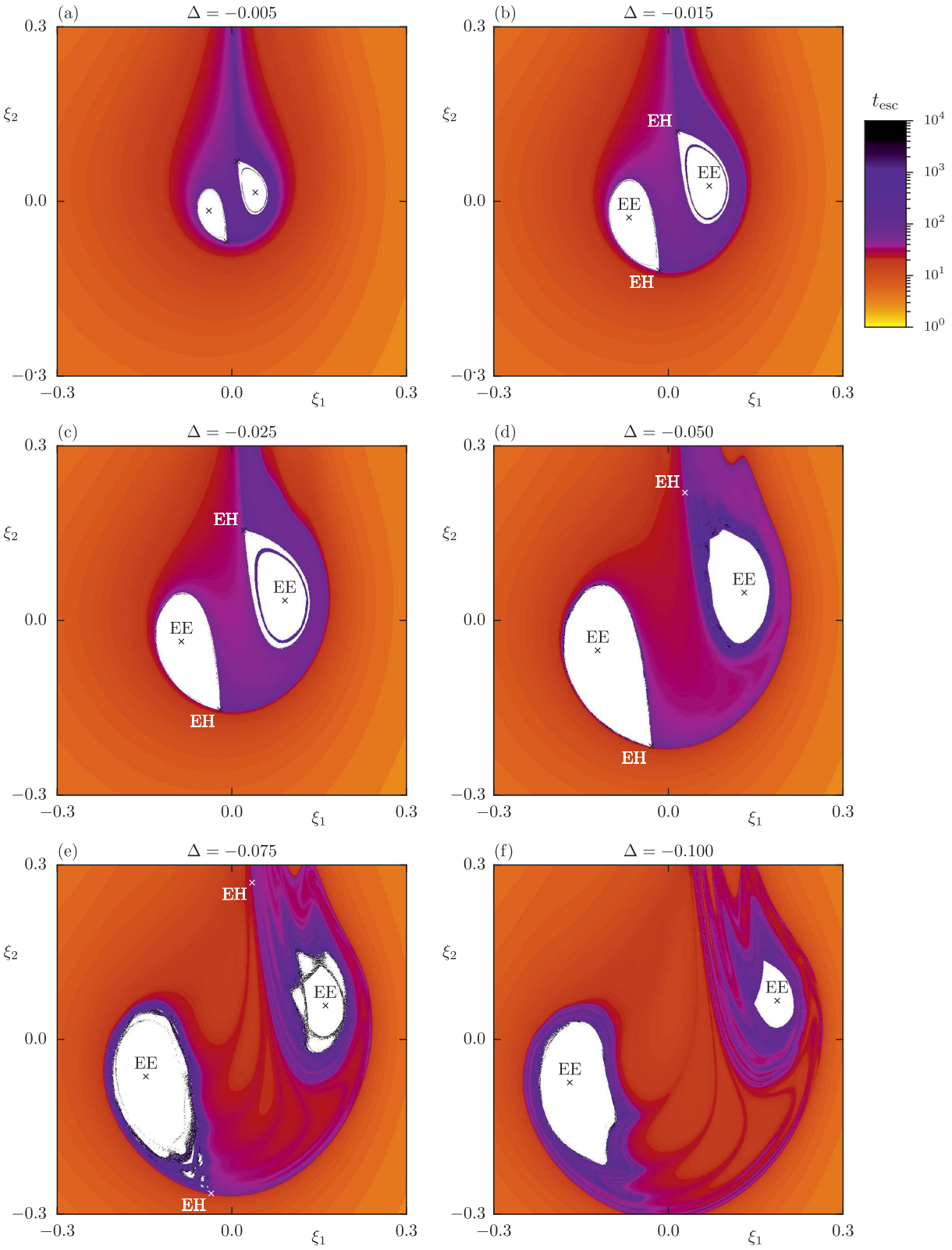

Fig. 3. Escape time plots with the parameters of (3.6) for six values of Δ, $(\alpha, \mu, \delta) = (1, 1, 0.5)$, and $\varepsilon_1 = \varepsilon_2 = 1$. Points on a 3000×3000 grid of initial conditions are iterated up to $t = 10^4$, and the escape time is encoded in the color scale shown at the top right. Points that do not escape are colored white.

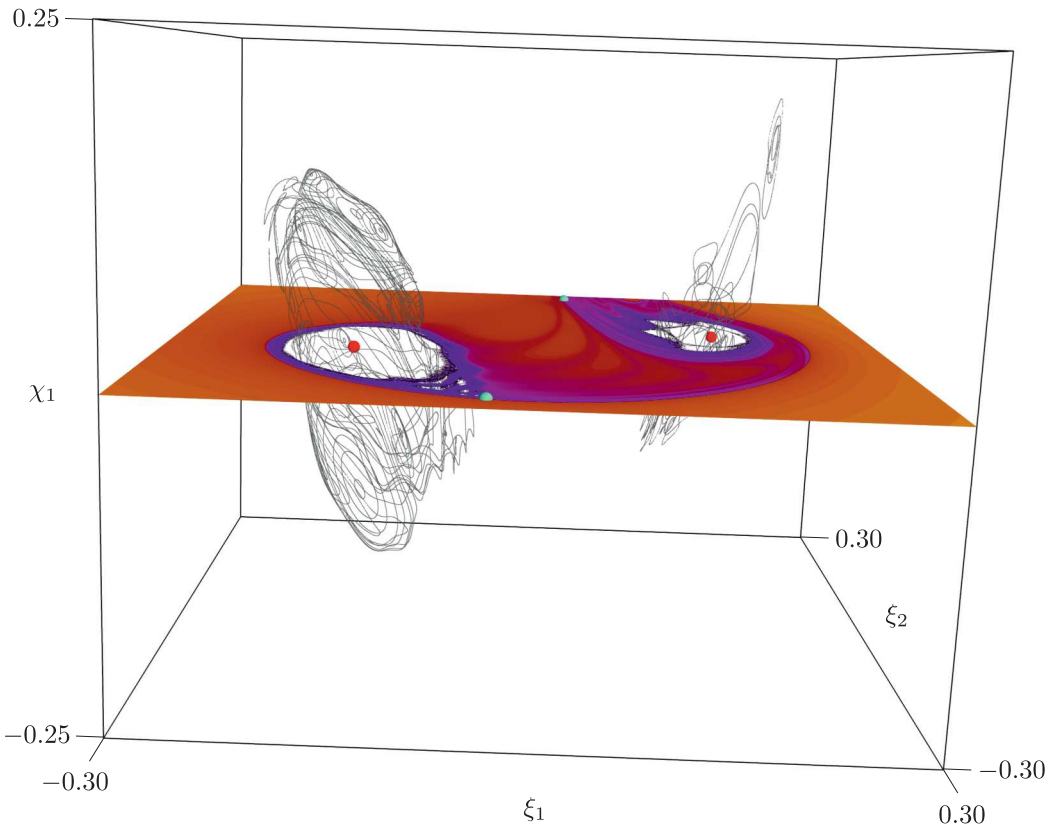

Fig. 4. 3D phase space slice for the Moser map and corresponding escape time plot in the $\eta = C\xi$ plane. The parameters are the same as Fig. 3e with $\Delta = -0.075$. Shown are several selected regular tori (grey curves) in the neighborhood of the EE fixed points. Each torus is represented by 10^4 points that fall in the slice (4.1) with $\epsilon = 10^{-6}$. The four fixed points are shown as small spheres: EE (red), EH (green). The coloring of the escape times is the same as in Fig. 3. For a rotating view, see Supplementary materials.

$\chi = 0$. In order to capture points on trajectories in the neighborhood of the fixed points, we define the slice

$$\Gamma_\epsilon = \left\{ (\xi_1, \xi_2, \chi_1, \chi_2) \;\middle|\; |\chi_2| \leqslant \epsilon \right\}, \tag{4.1}$$

which is a slight thickening of the 3D plane $\chi_2 = 0$. Whenever the points of an orbit, given by a sequence of points $(\xi_1, \xi_2, \chi_1, \chi_2)$, lie in this slice, the three nontrivial coordinates (ξ_1, ξ_2, χ_1) are displayed in a 3D plot. For further examples and detailed discussion see [33–36].

Figure 4 shows a 3D phase space slice plot combined with an escape time plot for a grid of initial conditions in the 2D-plane $\chi = 0$, for the quadfurcation of Fig. 2 when $\Delta = -0.075$, which corresponds to Fig. 3e. The elliptic-elliptic fixed points are surrounded by regions of predominantly regular motion. The intersections with the slice of a number of regular 2D tori are shown as grey curves. Various resonances lead to gaps of different sizes, and these are particularly visible in the tori that surround and approach the "left" EH fixed point (that with $\xi_1 < 0$). Between the tori one has chaotic motion in resonance channels that eventually may escape from the neigbhorhood of the EE fixed points. While the extent of each region with regular tori in the (ξ_1, ξ_2)-plane is approximately limited by the corresponding EH fixed point, the region containing tori seems to extend farther from the EE points in the χ_1 direction.

In contrast, there are two special cases for which Moser's map reduces to a pair of uncoupled Hénon maps (2.2). For example when $\varepsilon_1 = +1$, $c = 0$, and

$$C = \begin{pmatrix} \sqrt{3} & 0 \\ 0 & \frac{1}{\sqrt{3}} \end{pmatrix},$$

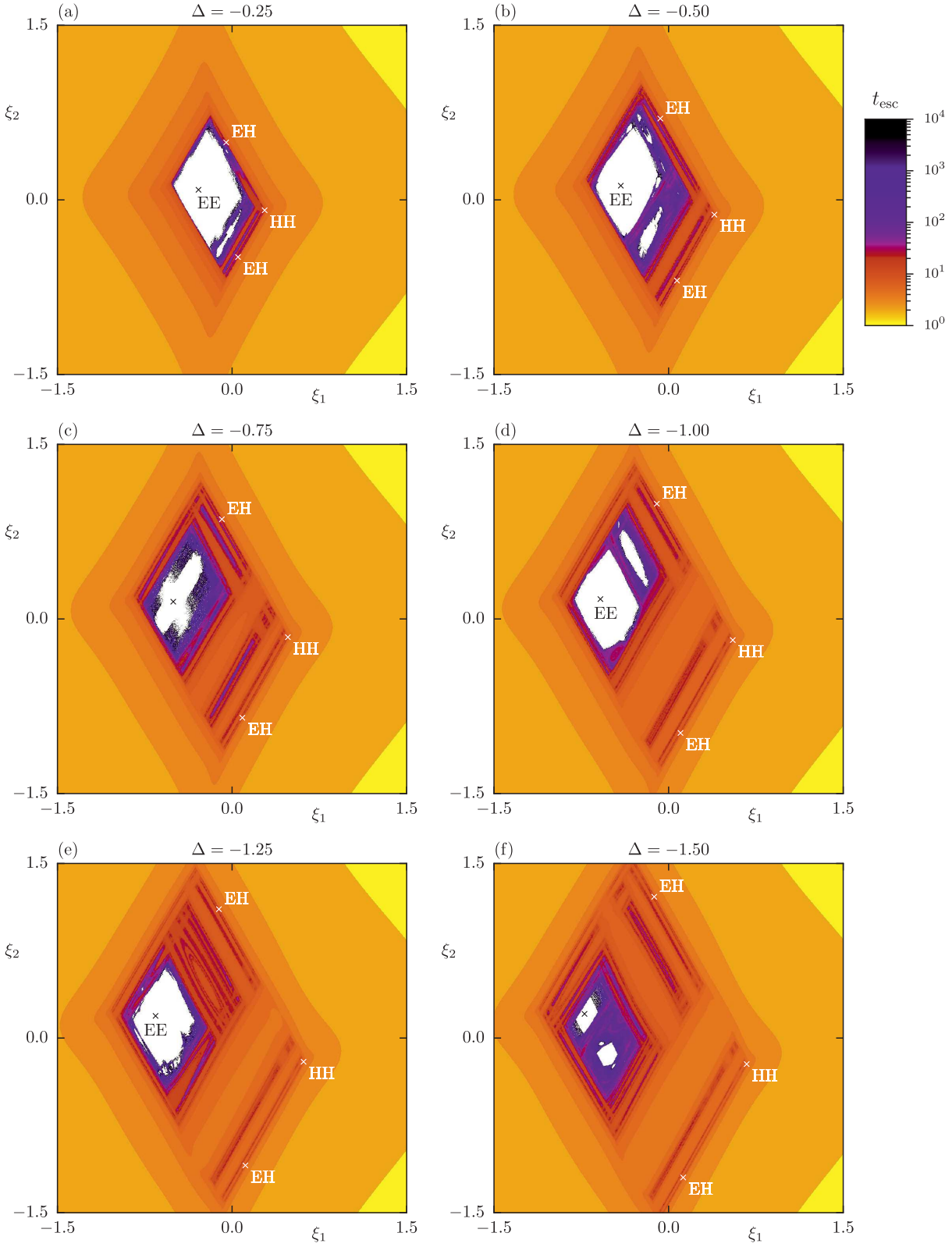

Fig. 5. Escape time plots for six values of Δ with $(a, b, c) = \Delta(1, -0.2, -0.1)$, $(\alpha, \mu, \delta) = (\sqrt{3}, 0, 1/\sqrt{3})$, and $\varepsilon_1 = \varepsilon_2 = 1$. Points on a 3000×3000 grid of initial conditions are iterated up to $t = 10^4$, and the escape time is encoded in the color scale shown at the top right. Points that do not escape up to $t = 10^4$ are colored white.

then the Moser map is equivalent (after a coordinate change) to two Hénon maps with $a_{\mathrm{h}1} = 1 + a - \sqrt{3}b$ and $a_{\mathrm{h}2} = 1 + a + \sqrt{3}b$. In this case the quadfurcation, at $a = b = 0$, corresponds to simultaneous saddle-center bifurcations of the individual Hénon maps, creating four fixed points of types EE, EH, EH and HH. Note that this quadfurcation occurs at the point $(A, B) = (4, 6)$ where there is a quadruplet of unit eigenvalues. When the parameter c is nonzero, these maps become coupled, but when c is small, the stability of the four fixed points is unchanged. As an illustration, a sequence of escape time plots for the path $(a, b, c) = \Delta(1, -0.2, -0.1)$ through this quadfurcation is shown in Fig. 5. The coupling is rather weak so that the product structure of the two 2D Hénon maps, as shown in Fig. 1, corresponding to $(a, b) = (-1, 0.2)$ and $c = 0$, is still visible. Specifically, the dynamics along the line connecting the EE fixed point to the lower EH fixed point in Fig. 5d is similar to that on the diagonal $y = x$ of the 2D map shown in Fig. 1a, and would be identical if c were 0. Similarly, the dynamics along the line connecting the EE fixed point to the upper EH fixed point is governed by that shown in Fig. 1b along its diagonal, $y = x$. In particular, the splitting of the white region of non-escaping points is caused by the stochastic motion around the period 5-island in the 2D map. This is also reflected in the structure of regular tori displayed in the 3D phase space slice plot shown in Fig. 6, where the resonance leads to several small regions with regular tori. Again the EE fixed point is surrounded by many regular tori shown as grey curves.

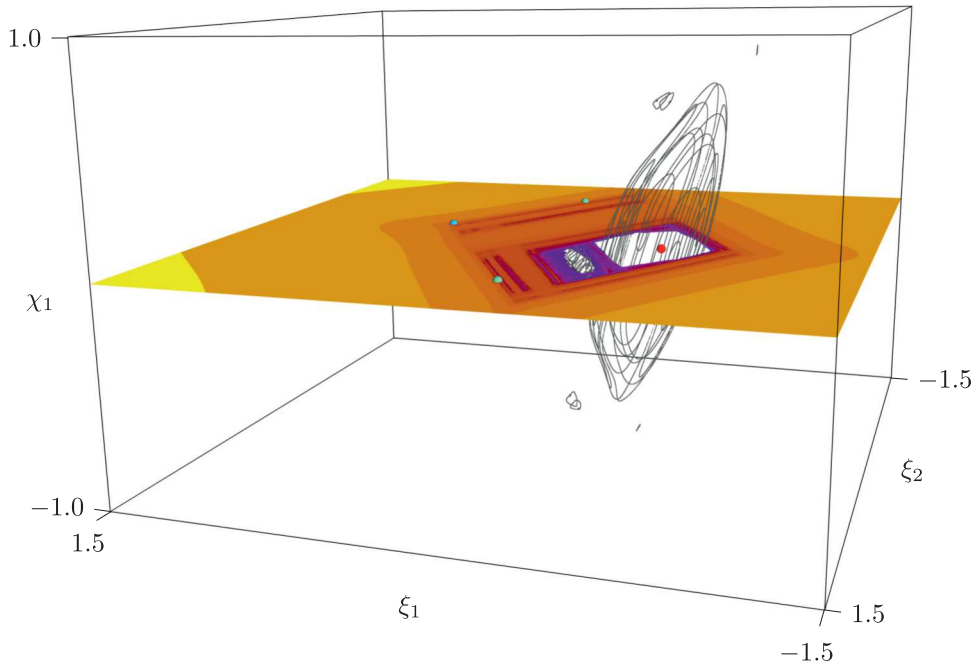

Fig. 6. 3D phase space slice for the weakly coupled Moser map and corresponding escape time plot in the $\eta = C\xi$ plane. Parameters are the same as in Fig. 5d with $\Delta = -1$. Shown are several selected regular tori (grey curves) near the EE fixed point. Each torus is represented by 10^4 points in the slice (4.1) with $\epsilon = 10^{-6}$. The four fixed points are shown as small spheres: EE (red), EH (green), and HH (blue). The coloring of the escape times is the same as in Fig. 5. For a rotating view, see Supplementary materials.

5. SOME IMPLICATIONS AND DISCUSSION

Our investigation of Moser's quadratic symplectic map in $\mathbb{R}^4$ reveals that for the quadfurcation, in which four fixed points are created from none, there are several distinct possibilities; one is the expected combination of two uncoupled Hénon maps, leading to one EE, two EH, and one HH fixed points, illustrated in Figs. 5 and 6. This case also describes accelerator mode islands [37, 38] that are born for the 4D standard map (Froeschlé's map [39]) when the coupling is small. Here the local dynamics reduces to a coupled version of a pair of Hénon maps [3].

Perhaps more surprising is the quadfurcation that creates two pairs of EE and EH fixed points, as illustrated in Figs. 3 and 4, which is only possible when different degrees of freedom are coupled.

An interesting question is whether there are cases of the Moser map that are integrable. Some examples of integrable area-preserving maps were found by Suris [40], and, for four-dimensions, by McLachlan [41]. None of these are quadratic maps, however. Near the quadfurcation, the Moser map can be approximated by the flow of a Hamiltonian system [3], so in this limit the Moser map has one invariant: the energy. In the 2D case, e. g., for the Hénon map, this is enough to imply that the limit is integrable. This also applies to the special 4D case mentioned above, when the Moser map is equivalent to a pair of uncoupled Hénon maps. More typically, the limiting Hamiltonian flow at the quadfurcation point is not expected to be integrable as it should not have a second invariant. Nevertheless there are known cases of two-degree-of-freedom, quadratic Hamiltonian flows that are integrable (and not obviously separable), e. g., the Hénon – Heiles relatives studied in [42], and thus there should be certain special parameters of the Moser map that have such a limit.

It will also be interesting in future research to do detailed studies of accelerator mode islands in the fully coupled 4D case, to study in more detail the stickiness and survival time statistics for Moser's map in $\mathbb{R}^4$, and to investigate what analogues of quadfurcation occur in higher dimensions.

ACKNOWLEDGMENTS

JDM acknowledges support from the U.S. National Science Foundation under grant DMS-1812481, and as Dresden Senior Fellow at the Technische Universität Dresden. AB acknowledges support by the Deutsche Forschungsgemeinschaft under grant KE 537/6–1. The visualizations of the 3D phase space slices were created using MAYAVI [43].

REFERENCES

1. Moser, J., On Quadratic Symplectic Mappings, *Math. Z.,* 1994, vol. 216, no. 3, pp. 417–430.
2. Hénon, M., A Two-Dimensional Mapping with a Strange Attractor, *Commun. Math. Phys.,* 1976, vol. 50, no. 1, pp. 69–77.
3. Bäcker, A. and Meiss, J. D., Elliptic Bubbles in Moser's 4D Quadratic Map: The Quadfurcation, arXiv:1807.06074 (2018).
4. Wisdom, J. and Holman, M., Symplectic Maps for the N-Body Problem, *Astron. J.,* 1991, vol. 102, no. 4, pp. 1528–1538.
5. Murray, N. and Holman, M., The Role of Chaotic Resonances in the Solar System, *Nature,* 2001, vol. 410, no. 6830, pp. 773–779.
6. Cincotta, P. M., Arnold Diffusion: An Overview through Dynamical Astronomy, *New Astron. Rev.,* 2002, vol. 46, no. 1, pp. 13–39.
7. Contopoulos, G. and Harsoula, M., 3D Chaotic Diffusion in Barred Spiral Galaxies, *Mon. Not. R. Astron. Soc.,* 2013, vol. 436, no. 2, pp. 1201–1214.
8. Páez, R. I. and Efthymiopoulos, Ch., Trojan Resonant Dynamics, Stability, and Chaotic Diffusion, for Parameters Relevant to Exoplanetary Systems, *Celest. Mech. Dyn. Astr.,* 2015, vol. 121, no. 2, pp. 139–170.
9. Daquin, J., Rosengren, A. J., Alessi, E. M., Deleflie, F., Valsecchi, G. B., and Rossi, A., The Dynamical Structure of the MEO Region: Long-Term Stability, Chaos, and Transport, *Celest. Mech. Dyn. Astr.,* 2016, vol. 124, no. 4, pp. 335–366.
10. Warnock, R. L. and Ruth, R. D., Long-Term Bounds on Nonlinear Hamiltonian Motion, *Physica D,* 1992, vol. 56, nos. 2–3, pp. 188–215.
11. Dumas, H. S. and Laskar, J., Global Dynamics and Long-Time Stability in Hamiltonian Systems via Numerical Frequency Analysis, *Phys. Rev. Lett.,* 1993, vol. 70, no. 20, pp. 2975–2979.
12. Robin, D., Steier, C., Laskar, J., and Nadolski, L., Global Dynamics of the Advanced Light Source Revealed through Experimental Frequency Map Analysis, *Phys. Rev. Lett.,* 2000, vol. 85, no. 3, pp. 558–561.
13. Papaphilippou, Y., Detecting Chaos in Particle Accelerators through the Frequency Map Analysis Method, *Chaos,* 2014, vol. 24, no. 2, 024412, 29 pp.
14. Howard, J. E., Lichtenberg, A. J., Lieberman, M. A., and Cohen, R. H., Four-Dimensional Mapping Model for Two-Frequency Electron Cyclotron Resonance Heating, *Physica D,* 1986, vol. 20, nos. 2–3, pp. 259–284.
15. Gaspard, P. and Rice, S. A., Hamiltonian Mapping Models of Molecular Fragmentation, *J. Phys. Chem.,* 1989, vol. 93, no. 19, pp. 6947–6957.
16. Gillilan, R. E. and Ezra, G. S., Transport and Turnstiles in Multidimensional Hamiltonian Mappings for Unimolecular Fragmentation: Application to van der Waals Predissociation, *J. Chem. Phys.,* 1991, vol. 94, no. 4, pp. 2648–2668.

17. *Geometric Structures of Phase Space in Multidimensional Chaos: Applications to Chemical Reaction Dynamics in Complex Systems: In 2 Vols.,* M. Toda, T. Komatsuzaki, T. Konishi, R. S. Berry, S. A. Rice (Eds.), Adv. Chem. Phys., vol. 130, Hoboken, N.J.: Wiley, 2005.
18. Gekle, S., Main, J., Bartsch, Th., and Uzer, T., Extracting Multidimensional Phase Space Topology from Periodic Orbits, *Phys. Rev. Lett.,* 2006, vol. 97, no. 10, 104101, 4 pp.
19. Waalkens, H., Schubert, R., and Wiggins, S., Wigner's Dynamical Transition State Theory in Phase Space: Classical and Quantum, *Nonlinearity,* 2008, vol. 21, no. 1, R1–R118.
20. Manikandan, P. and Keshavamurthy, S., Dynamical Traps Lead to the Slowing Down of Intramolecular Vibrational Energy Flow, *Proc. Natl. Acad. Sci. USA,* 2014, vol. 111, no. 40, pp. 14354–14359.
21. Hénon, M., Numerical Study of Quadratic Area-Preserving Mappings, *Quart. Appl. Math.,* 1969, vol. 27, pp. 291–312.
22. Devaney, R. and Nitecki, Z., Shift Automorphisms in the Hénon Mapping, *Commun. Math. Phys.,* 1979, vol. 67, pp. 137–146.
23. Broucke, R., Stability of Periodic Orbits in the Elliptic, Restricted Three-Body Problem, *AIAA J.,* 1969, vol. 7, no. 6, pp. 1003–1009.
24. Howard, J. E. and MacKay, R. S., Linear Stability of Symplectic Maps, *J. Math. Phys.,* 1987, vol. 28, no. 5, pp. 1036–1051.
25. Broer, H. W. and Sevryuk, M. B., KAM Theory: Quasi-Periodicity in Dynamical Systems, in *Handbook of Dynamical Systems: Vol. 3,* H. W. Broer, B. Hasselblatt, F. Takens (Eds.), Amsterdam: Elsevier, 2010, pp. 249–344.
26. Moser, J., On Invariant Curves of Area-Preserving Mappings of an Annulus, *Nachr. Akad. Wiss. Göttingen Math.-Phys. Kl. II,* 1962, vol. 1962, pp. 1–20.
27. Delshams, A. and Gutiérrez, P., Estimates on Invariant Tori near an Elliptic Equilibrium Point of a Hamiltonian System, *J. Differential Equations,* 1996, vol. 131, no. 2, pp. 277–303.
28. Eliasson, L. H., Fayad, B., and Krikorian, R., KAM-Tori near an Analytic Elliptic Fixed Point, *Regul. Chaotic Dyn.,* 2013, vol. 18, no. 6, pp. 801–831.
29. Arnold, V. I., On the Nonstability of Dynamical Systems with Many Degrees of Freedom, *Soviet Math. Dokl.,* 1964, vol. 5, no. 3, pp. 581–585; see also: *Dokl. Akad. Nauk SSSR,* 1964, vol. 156, no. 1, pp. 9–12.
30. Lochak, P., Arnold Diffusion: A Compendium of Remarks and Questions, in *Hamiltonian Systems with Three or More Degrees of Freedom (S'Agaró, 1995),* C. Simó (Ed.), NATO Adv. Sci. Inst. Ser. C Math. Phys. Sci., vol. 533, Dordrecht: Kluwer, 1999, pp. 168–183.
31. Delshams, A. and Huguet, G., A Geometric Mechanism of Diffusion: Rigorous Verification in a priori Unstable Hamiltonian Systems, *J. Differential Equations,* 2011, vol. 250, no. 5, pp. 2601–2623.
32. Dumas, H. S., *The KAM Story: A Friendly Introduction to the Content, History, and Significance of Classical Kolmogorov – Arnold – Moser Theory,* Hackensack, N.J.: World Sci., 2014.
33. Richter, M., Lange, S., Bäcker, A., and Ketzmerick, R., Visualization and Comparison of Classical Structures and Quantum States of Four-Dimensional Maps, *Phys. Rev. E,* 2014, vol. 89, no. 2, 022902, 12 pp.
34. Lange, S., Richter, M., Onken, F., Bäcker, A., and Ketzmerick, R., Global Structure of Regular Tori in a Generic 4D Symplectic Map, *Chaos,* 2014, vol. 24, no. 2, 024409, 11 pp.
35. Onken, F., Lange, S., Ketzmerick, R., and Bäcker, A., Bifurcations of Families of 1D-Tori in 4D Symplectic Maps, *Chaos,* 2016, vol. 26, no. 6, 063124, 13 pp.
36. Firmbach, M., Lange, S., Ketzmerick, R., and Bäcker, A., Three-Dimensional Billiards: Visualization of Regular Structures and Trapping of Chaotic Trajectories, *Phys. Rev. E,* 2018, vol. 98, no. 2, 022214, 18 pp.
37. Izrailev, F. M. and Chirikov, B. V., Some Numerical Experiments with a Nonlinear Mapping: Stochastic Component, in *Proc. Colloques Internationaux du CNRS (Toulouse, 1973), No. 229,* pp. 409–428.
38. Kook, H.-T. and Meiss, J. D., Diffusion in Symplectic Maps, *Phys. Rev. A (3),* 1990, vol. 41, no. 8, pp. 4143–4150.
39. Froeschle, C., On the Number of Isolating Integrals in Systems with Three Degrees of Freedom, *Astrophys. Space Sci.,* 1971, vol. 14, no. 1, pp. 110–117.
40. Suris, Yu. B., Integrable Mappings of the Standard Type, *Funct. Anal. Appl.,* 1989, vol. 23, no. 1, pp. 74–76; see also: *Funktsional. Anal. i Prilozhen.,* 1989, vol. 23, no. 1, pp. 84–85.
41. McLachlan, R. I., Integrable Four-Dimensional Symplectic Maps of Standard Type, *Phys. Lett. A,* 1993, vol. 177, no. 3, pp. 211–214.
42. Bountis, T., Segur, H., and Vivaldi, F., Integrable Hamiltonian Systems and the Painlevé Property, *Phys. Rev. A (3),* 1982, vol. 25, no. 3, pp. 1257–1264.
43. Ramachandran, P. and Varoquaux, G., Mayavi: 3D Visualization of Scientific Data, *Comput. Sci. Eng.,* 2011, vol. 13, no. 2, pp. 40–51.